Obtaining more energetic modelocked pulses from a SESAM-based fiber laser

SHAOKANG WANG,[1,*] CHAORAN TU,[1] SEYED EHSAN JAMALI MAHABADI,[1] STEFAN DROSTE,[2] LAURA C. SINCLAIR,[2] IAN CODDINGTON,[2] NATHAN R. NEWBURY,[2] THOMAS F. CARRUTHERS,[1] AND CURTIS R. MENYUK[1]

[1]*Department of Computer Science and Electrical Engineering, University of Maryland, Baltimore County, 1000 Hilltop Circle, Baltimore, MD 21250, USA*
[2]*National Institute of Standards and Technology, 325 Broadway, Boulder, CO 80305, USA*
*swan1@umbc.edu

Abstract: A major design goal for femtosecond fiber lasers is to increase the output power but not at the cost of increasing the noise level or narrowing the bandwidth. Here, we perform a computational study to optimize the cavity design of a femtosecond fiber laser that is passively modelocked with a semiconductor saturable absorbing mirror (SESAM). We use dynamical methods that are more than a thousand times faster than standard evolutionary methods. We show that we can obtain higher pulse energies and hence higher output powers by simultaneously increasing the output coupling ratio, the gain, and the anomalous group delay dispersion. We can obtain output pulses that are from 5 to 15 times the energy of the pulse in the current experimental design with no penalty in the noise level or bandwidth.

1. Introduction

During the past two decades, passively modelocked fiber lasers have become increasingly attractive sources for producing robust, low-noise frequency combs [1–8]. The key design problem for passively modelocked lasers is to find a region in the laser's experimentally-adjustable parameter space where the laser can operate stably and optimize the design to produce an output pulse with a desirable profile—for example, a pulse with high peak/average output power, a short pulse duration, and/or low amplitude and timing jitter. Adjustable parameters may include the cavity length, the cavity dispersion, the cavity loss including the output coupling, and the cavity gain. The cavity gain as a function of frequency typically depends on the pump power, pump wavelength, and gain material.

In this paper, we present a detailed computational study to optimize the cavity design of a femtosecond fiber laser with a repetition frequency of 300 MHz that is passively modelocked using a semiconductor saturable absorbing mirror (SESAM). SESAMs are now widely used in order to modelock solid-state lasers and waveguide lasers, as well as fiber lasers [9–14]. Typically, the response time of these saturable absorbers is longer than the output pulse duration, which leads to experimentally-observed wake mode sidebands [15–17]. The laser that we optimize is similar to the laser that was reported in [11]. This work extends our prior preliminary work on optimization [18,19].

To carry out this optimization, we use a unique set of computational tools based on dynamical systems theory [20–22]. These dynamical methods yield the stable operating parameter region [20] and the noise performance [21,22] orders-of-magnitude faster than would be possible using conventional evolutionary methods [16,18]. These methods make it possible to carry out a three-dimensional parameter optimization in which we vary the unsaturated gain of the doped fiber, the cavity dispersion, and the output coupling. A more detailed computational study of the

efficiency of the dynamical methods can be found in [22], in which we show that to evaluate the noise of a soliton laser, the CPU time cost is 1000 times less using the dynamical methods than is the case for traditional Monte-Carlo-based evolutionary methods. We will show that we can obtain a more energetic, stable, and broadband output pulse as we increase the output coupling ratio up to 40%. Meanwhile, the wake mode sidebands never rise more than 5% above the broadband optical relative intensity noise (RIN) level that is due to amplified spontaneous noise emission into continuous waves. Indeed, the optical RIN actually decreases, although the absolute magnitude of the wake mode sidebands increases. We explain the physics behind this somewhat unintuitive result.

Our optimization procedure has two significant limitations. First, we use an averaged model that neglects the changes that occur during one round trip in the laser. Second, we use a parabolic differential gain model rather than taking into account the realistic gain profile in an erbium-doped fiber amplifier (EDFA). For that reason, we validated the starting parameters of our averaged model by comparison to experiments, and we verified the results of our optimization in two selected cases using standard evolutionary simulations with a lumped model in which all the laser components are modeled as realistically as possible, including the EDFA. In our evolutionary simulations, we allowed an initial pulse to circulate for several thousand round trips until it stabilized. Both cases that we verified had an output coupling of 20%, and both produced an increase in the output power relative to the current experimental system by a factor of about five with a comparable pulse duration and negligible sidebands.

We obtained our best results by simultaneously increasing the cavity gain and anomalous dispersion along with the output coupling. At the limits of the parameter range that we considered with an output coupling of 40%, our optimization procedure produced a pulse with fifteen times the pulse energy, half the pulse duration, and a lower sideband level relative to the output power. Achieving the limits of the parameter range that we considered would require the use of an erbium-ytterbium co-doped fiber (EYDF) to achieve the increase in the gain and photonic crystal fiber (PCF) to achieve the increased anomalous dispersion at 1550 nm. Fibers that achieve the limits of our parameter range have been demonstrated in laboratory experiments [23]. What is more important than the exact quantitative results is that our optimization procedure provides a roadmap to produce higher energy pulses without sacrificing bandwidth or noise performance, while pointing to the physics that yields the improved performance.

The remainder of this paper is organized as follows: In Sec. 2, we introduce the experimental configuration that we model and describe the averaged model that we use in our optimization. In Sec. 3, we present our model validations in which we compare the pulse parameters and sideband levels for both the averaged and lumped models to the experimental results. In Sec. 4, we present our three-dimensional parameter optimization. In Sec. 5, we present our verification of the averaged model in two selected cases using our lumped model. In Sec. 6, we discuss the physics behind our optimization results, and we conclude.

2. SESAM fiber laser and the averaged model

In Fig. 1, we show an illustration of the experimental laser configuration that is the starting point for our optimization [11]. It is built with telecom-grade polarization-maintaining (PM) components, and it is able to generate a highly stable 300-MHz frequency comb. The cavity components include a 22.4-cm-long segment of highly-doped erbium-doped fiber (EDF), a 12.2-cm-long segment of PM fiber, and a SESAM (BATOP SAM-1550), with a response time of 2 ps, which is connected to the EDF by a fiber-optic physical contact coupler (FC/PC). Both fibers have anomalous dispersion. In current experiments, the single mode fiber is Corning PM-1550 and the erbium-doped fiber is Nufern PM-ESF-7/125. The pump signal is a 980-nm continuous wave laser, and the pump is launched into the cavity via a wavelength-division-multiplexing

(WDM) coupler. The output pulse duration is 300 fs, the roundtrip time is 3.3 ns, and the gain response is 1–10 ms.
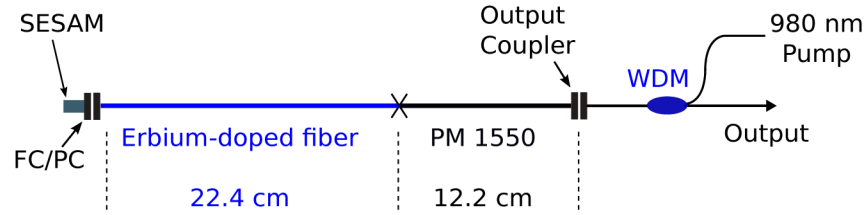

Fig. 1. Illustration of the experimental SESAM fiber laser configuration.

In this work, we use an averaged model [16,21] combined with a unique set of computational codes based on dynamical methods to carry out the optimization. The dynamical methods combine boundary-tracking algorithms to determine the precise region in the adjustable parameter space where stable pulse solutions exist [20] and spectral methods [21,22] to determine the noise performance. A modelocked pulse can be viewed as a stationary solution or an equilibrium of a nonlinear dynamical system. If any possible perturbation grows exponentially, then the system is unstable. The stability can be determined by solving a linear eigenvalue problem. Once a single modelocked solution has been found for a single set of parameters either analytically or using the evolution equations, we can rapidly trace the solution as parameters vary by solving a root-finding problem and determine the solution's stability and evaluate the noise without solving the evolution equations. This approach allows us to rapidly determine the existence, stability, and noise of pulses over a broad parameter range. The computational speed of these methods can be thousands of times faster [22] than methods based on standard evolutionary methods that follow a pulse for many round trips in a laser cavity and that use Monte Carlo simulations to determine the noise performance. They have made it possible to carry out the three-dimensional parameter optimization in this study.

Traditionally, characterizing the noise performance requires solving the evolution equations and Monte-Carlo simulations. As the dimensionality of the optimization grows, this approach can become overwhelmingly computationally expensive. The advantage of the dynamical methods over the traditional Monte-Carlo simulations is the computational efficiency. The calculation that we show later in Fig. 3, which are based on the traditional Monte-Carlo simulations, takes hours or even days of computer time. By comparison, the calculations that we show later in Figs. 7 and 10 take only a few minutes. A more detailed description of the dynamical method and its computational efficiency can be found in [22].

The averaged model that we use is a variant of the Haus modelocking equation [1] that was introduced in [15–17]. The evolution of the wave envelope is described by

$$
\begin{aligned}
T_R \frac{\partial u}{\partial T} = & -i\phi u + t_s \frac{\partial u}{\partial t} + \frac{g(|u|)}{2}\left(1 + \frac{1}{2\omega_g^2}\frac{\partial^2}{\partial t^2}\right)u - \frac{l}{2}u \\
& -i\frac{\beta''}{2}\frac{\partial^2 u}{\partial t^2} + i\gamma|u|^2 u - \frac{\rho}{2}n(t)u + s(t, T),
\end{aligned}
\tag{1}
$$

where T_R is the round trip time, T is the slow time of propagation, t is the retarded fast time, $u(t, T)$ is the slowly varying field envelope, and each operator on u on the right-hand side of Eq. (1) is averaged over one round trip. The time t_s is the time shift in the fast time t of the pulse centroid $t_c = \int t'|u|^2 dt' / \int |u|^2 dt'$, ϕ is the phase change, g is the saturated gain, ω_g is the gain bandwidth, β'' is the group-delay dispersion, γ is the Kerr coefficient, and ρ is the peak saturable

coefficient of the SESAM. We use l to represent linear loss in the cavity, so that

$$l = l_{\text{rem}} - \ln(1 - t_{\text{out}}), \tag{2}$$

where t_{out} is the output coupling ratio and l_{rem} is the remainder of the loss in the cavity. The average output power increases as t_{out} increases. We assume that the recovery time of the gain is significantly longer than the round-trip time, so that the gain $g(|u|)$ may be written

$$g(|u|) = \frac{g_0}{1 + w_0/(P_{\text{sat}} T_R)}, \tag{3}$$

where g_0 is the unsaturated gain, w_0 is the intra-cavity pulse energy, and P_{sat} is the saturation power of the doped fiber. The term $(g/2)[1 + (\omega_g^2/2)\partial^2/\partial t^2]$ in Eq. (1) corresponds to a parabolic differential gain response. In simulations, we modified g_0 to ensure that the output power P_{out} matches the experimental output powers.

We use a two-level model of the SESAM where n is the ratio of the lower level population to the total population of the SESAM [17] (Here, we correct Eq. (3) in [16] and Eq. (8) in [22]),

$$\frac{dn(t)}{dt} = \frac{1-n}{T_A} - \frac{|u(t)|^2}{w_A}n, \quad n(-T_R/2) = 1, \tag{4}$$

where we assume that the response time $T_A \ll T_R$ and w_A is the saturation energy of the SESAM.

The noise source $s(t, T)$ is defined by [24]

$$\langle s(t, T)s^*(t', T') \rangle = g(|u_0|)h\nu_0 T_R \delta(t - t')\delta(T - T'), \tag{5}$$

where the operator $\langle \cdot \rangle$ represent the ensemble average, the symbol $*$ represents complex conjugation, h is Planck's constant, ν_0 is the central frequency of the laser's output pulse, and $\delta(\cdot)$ is the Dirac delta function.

The phase shift and time shift per round trip, ϕ_s and t_s have no impact on the intensity profile of the modelocked pulse solution due to the phase and time invariance of Eq. (1). When studying modelocking analytically [24] or using standard evolutionary simulations [25], it is conventional to set these parameters equal to zero. When using dynamical methods, it is more convenient to determine them in parallel with the stationary solution so that it is strictly stationary [20–22].

2.1. Wake mode instability

Here, we provide a brief introduction to the wake mode instability (WMI). A more detailed description of the wake mode instability can be found in [16].

The WMI is a mechanism that breaks the modelocked state of the comb laser. This instability is introduced due to the long recovery time of the slow saturable absorber—in our case, the SESAM. Kärtner et al. [17] used soliton perturbation theory to study the stability of this type of lasers, and they first predicted the WMI. We later examined the WMI computationally using realistic pulse parameters [18] in order to determine the parameters at which it sets in and its evolution. We found that the WMI leads to a quasi-periodic leapfrog process in which a newly generated pulse in the wake of the existing pulse steals its energy. The WMI sets a lower limit on the magnitude of the group velocity dispersion (in this paper, β''), and an upper limit on the pump power (in this paper, the unsaturated gain, g_0), which in turn set a lower limit on the pulse duration and an upper limit on the pulse energy [18,19].

3. Validation of the averaged and lumped models

Our starting point is to validate both our averaged and lumped model by comparison to the experiments for our reference laser. In the lumped model, each cavity component operates

independently on the optical pulse, and the operations are cascaded consecutively. As a consequence, the pulse profile varies as the pulse propagates through the cavity components during one round trip. We show an example of the pulse propagation in Visualization 1. The averaged model assumes that the variations of the pulse profile during one round trip are small enough to be ignored. While the lumped model is too slow to be used for optimization, we will later use it to verify that the increase in pulse energy that the averaged model predicts is realistic given the limitations of the averaged model. The lumped model contains many parameters, not all of which are known. The averaged model parameters cannot be obtained even in principle by simply averaging over the position in the laser since the impact of dispersion is affected by the pulse evolution [26]. It is necessary to make reasonable choices. We chose our unknown parameters in order to ensure that the average output power and the location of the sidebands in the radio frequency (RF) intensity spectrum match.

In Table 1, we list the parameters that we used in our averaged model, along with the output pulse duration τ_{out} and output average power P_{out} that is predicted by this model. We used the experimentally-measured values for T_R and β''. The variables T_A, ρ, and the SESAM contribution to l_{rem} are evaluated using the SESAM data sheet. The Kerr coefficient is obtained using $\gamma = 2\pi\kappa L/(\lambda A_{\text{eff}})$, where we estimate $\kappa = 2.5 \times 10^{-20} \, \text{m}^2/\text{W}$, the round trip fiber length $L = 70 \, \text{cm}$, $\lambda = 1560 \, \text{nm}$ is the central wavelength, and the average beam diameter for both the erbium-doped fiber and the single mode fiber as $9 \, \mu\text{m}$. We estimate the gain saturation power P_{sat} from relationship between the pump power and the output power, and we estimate the SESAM saturation energy using $w_A = \Phi_{\text{sat}} A_{\text{eff,SESAM}}$, where the saturation fluence is $\Phi_{\text{sat}} = 50 \, \mu\text{J/cm}^2$ and the measured spot size inside the SESAM is $A_{\text{eff,SESAM}} = 314 \, \mu\text{m}^2$. We select the values for g_0 and ω_g that provide the best agreement with the experimental output power P_{out} and the RF intensity spectrum. More details on the parameter selection may be found in [27].

Table 1. Parameter values that we use in Eqs. (1)–(5). We vary the values of g_0, β'', and t_{out} in the parameter study in Secs. 3 and 4.

$T_R = 3.33 \, \text{ns}$	$w_A = 157 \, \text{pJ}$	$P_{\text{sat}} = 9.01 \, \text{mW}$
$g_0 = 7.74$	$\rho = 0.073$	$\beta'' = -0.0144 \, \text{ps}^2$
$\omega_g = 30 \, \text{ps}^{-1}$	$T_A = 2.00 \, \text{ps}$	$\gamma = 0.0011 \, \text{W}^{-1}$
$l_{\text{rem}} = 0.96$	$t_{\text{out}} = 9\%$	
$\tau_{\text{out}} = 254 \, \text{fs}$	$P_{\text{out}} = 4.9 \, \text{mW}$	

For our lumped model, we used the Giles-Desurvire model for the erbium-doped fiber [28]. The doping density for our validation study was $N_e = 3.47 \times 10^{25} \, \text{m}^{-3}$, and the core radius was $3.50 \, \mu\text{m}$. Other model parameters may be found in [27]. For our reference laser, corresponding to $g_0 = 7.74$, we used a pump power of $P_{\text{pump}} = 237 \, \text{mW}$.

Most other parameters are the same as in the averaged model. However, we used a dispersion of $-0.03 \, \text{ps}^2/\text{m}$ in the polarization-maintaining and gain fibers, which leads to a total round-trip dispersion that is somewhat larger than the dispersion that we used in the averaged model. Since the gain models are different and the amplitude varies during one round trip in the lumped model, which changes the effective dispersion in one round trip from the average dispersion [29], this difference is not surprising. In our verification studies, reported in Sec. 5, we scaled the dispersion by the same factor in both the averaged and lumped models when comparing the results.

The experimental system that we used as our starting point has a full-width half maximum (FWHM) pulse duration of about $\tau_{\text{out}} = 300 \, \text{fs}$, an average output of $P_{\text{out}} = 4.9 \, \text{mW}$ with an input pump power of $237 \, \text{mW}$. With our corresponding reference laser parameters, we have for the averaged model $P_{\text{out}} = 4.9 \, \text{mW}$ and $\tau_{\text{out}} = 254 \, \text{fs}$. We have for the lumped model $P_{\text{out}} = 4.8$

mW and $\tau_{\text{out}} = 311$ fs. We observe that the pulse duration is somewhat smaller in the averaged model—a result that we will see repeated in the verification studies that are reported in Sec. 5.

We now turn to validation of our averaged and lumped models by comparing the sidebands to the experimentally-measured sidebands. In order to do that, we must model the measurement system in addition to the laser [27].

In Fig. 2, we illustrate the model of the measurement system. The pulse dynamics inside the laser cavity are described by Eqs. (1)–(5). We represent the pulse as a function of the fast time t inside a time window T_w. This window moves periodically inside the laser cavity along with the pulse, returning to the same point after one round-trip time T_R. Inside the window, the pulse evolves as a function of the slow time T. Thus, the pulse $u(t, T)$ is a function of both t and T. We use a modified split-step Fourier method [25] to solve Eqs. (1)–(5).
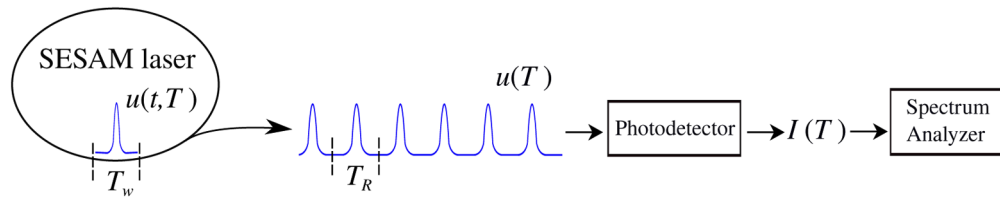

Fig. 2. Illustration of the RF spectrum measurement. We unwrap the optical field $u(t, T)$ to produce $u(T)$ at the output port, where T_w is the computational time window and T is the roundtrip time.

As shown in Fig. 2, once the pulse exits the cavity, we "unwrap" the periodic train of pulses that appear at the output port and obtain a function of a single time variable $u(T)$ which is the input to our photodetector model. The repetition frequency of the SESAM fiber laser is 300 MHz. The frequency components that we detect are below 100 MHz, which is far below the bandwidth of a high speed photodetector. Thus, in our computations, we set the output signal of the photodetector in Fig. 2 equal to the integrated energy over each round trip

$$I(T) = \begin{cases} \eta \int_{-T_R/2}^{T_R/2} |u(t, T)|^2 \mathrm{d}t, & T = 0, 1, 2, \ldots, \\ 0, & \text{otherwise.} \end{cases} \tag{6}$$

Since the calibration for the output current is unknown, we set $\eta = 1$ in our computations for convenience. The current $I(T)$ is the input to our spectrometer model. This model calculates the Fourier transform of $I(T)$ and then averages this transform inside frequency bins Δf that correspond to the spectrometer's resolution. A detailed description of the mathematical formulation of this model can be found in [27, Chapter 3].

In Fig. 3, we show a comparison of the sidebands in dB/Hz to the experimentally-measured RF intensity spectrum for both the averaged and lumped models. For both models, there is an unknown calibration factor that has to be adjusted. Hence, only the relative magnitude of the sidebands to the broadband noise is meaningful. We observe that the agreement of both models with the experimental spectrum is good. Both the sideband frequency and sideband power maximum increase as the pump power P_{pump} increases; we previously reported the increase in the sideband frequency in [16]. The laser becomes unstable when $P_{\text{pump}} > 255$ mW in the lumped model, corresponding to $g_0 > 8.4$ in the averaged model. This limit is consistent with the experiments. The sidebands in the RF spectrum are asymmetric, which indicates that there is a Fano-like contribution [30] of the continuous waves to the sidebands. This asymmetry is present in the averaged model, although it is less pronounced than in the lumped model or the experiments. The discrepancy is due to the limitations of the gain model in the averaged model. The dynamical methods that we use in the next section for optimization include the continuous wave contributions to the sidebands and exhibit the same asymmetry.
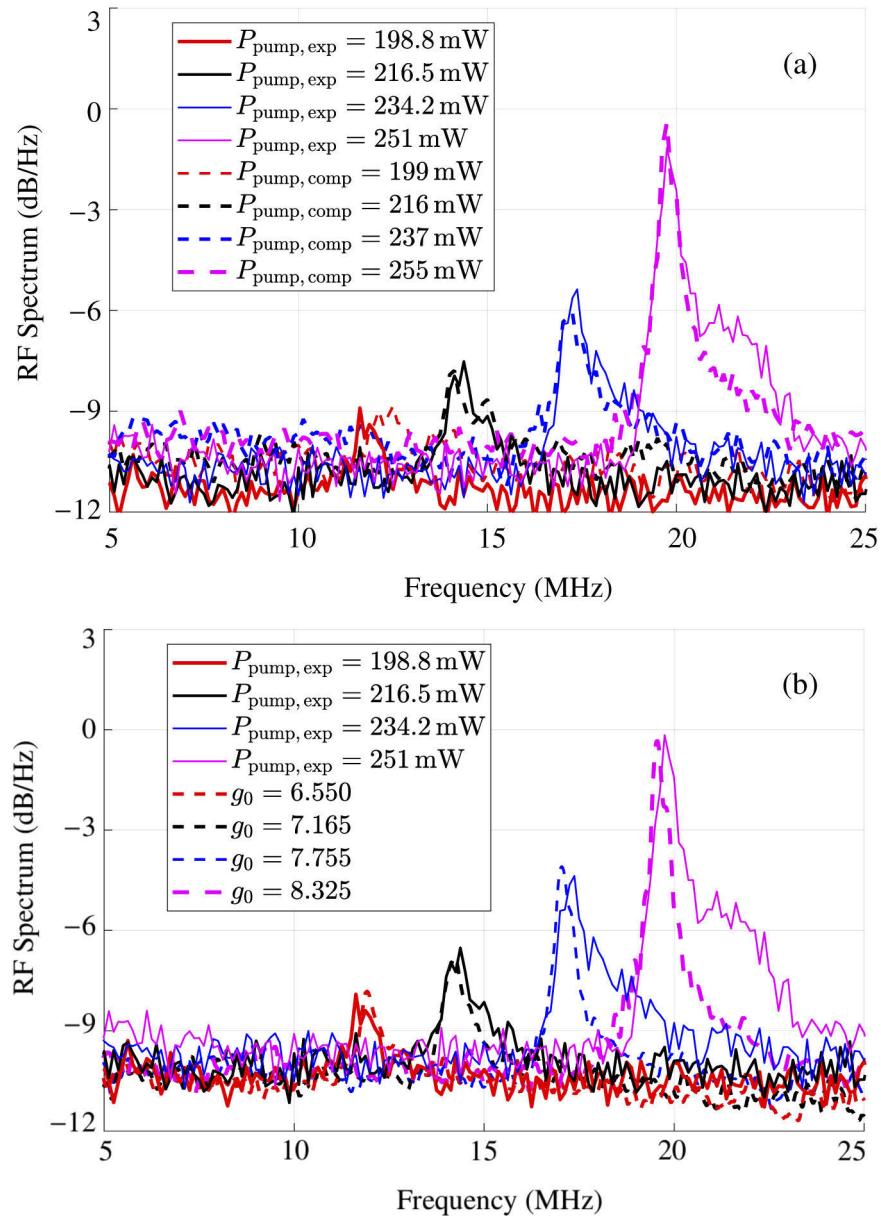
Fig. 3. Comparison of the experimentally-observed and computationally-calculated RF intensity spectrum using (a) the lumped model and (b) the averaged model, where g_0 is the unsaturated gain in our simulation that is defined in Eq. (3), while $P_{\text{pump, exp}}$ and $P_{\text{pump, comp}}$ are the pump power in experiments and in the lumped model, respectively [27].

4. Optimizing the laser cavity

Here, we carry out a three-dimensional optimization of the laser parameters in the averaged model, using the dynamical methods described in detail in [16,20–22,27]. The parameters in Table 1 that correspond to our reference laser are our starting point, and we vary the output coupling t_{out}, the unsaturated gain g_0, and the dispersion β'' . We chose to represent the change in the amplifier gain by only varying g_0 rather than varying both g_0 and P_{sat} in order to reduce the complexity of the optimization from four dimensions to three. This choice has no impact on the trends or the conclusions, which we verify in Sec. 5. We show an illustration of the parameter space that we vary in Fig. 4. We choose four different values of t_{out} (9%, 20%, 30%, and 40%). For a given value of t_{out}, we vary either g_0 or β'' and calculate the pulse energy w_0, from which we determine

$$P_{\text{out}} = t_{\text{out}} w_0 / T_R, \tag{7}$$

and we calculate the FWHM output pulse duration τ_{out}. We also calculate the optical power spectral density (PSD) of the energy, $S_w(f)$, from which we calculate the corresponding PSD in dBc (Here, we correct Eq. (6.2) on page 95 of [27]),

$$S_w(f)_{(\text{dBc})} = 10 \log_{10} \frac{S_w(f)}{w_0^2}. \tag{8}$$

The goals of our optimization study are to increase P_{out} while decreasing τ_{out} and decreasing the sideband maxima I_{sb}. We measured I_{sb} relative to the broadband noise due to amplified spontaneous emission into continuous waves.
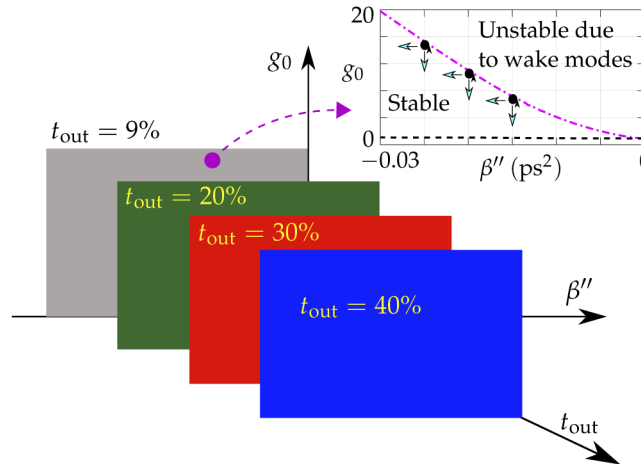

Fig. 4. An illustration of the parameter space, $(t_{\text{out}}, \beta'', g_0)$. As illustrated using arrows in the embedded picture, we monitor how the output parameters vary (as shown later in Figs. 6 and 7) as the system parameters g_0 and β'' vary.

In Fig. 5 and Table 2, we briefly summarize the optimization directions and the results. We mark four directions, $\mathcal{A}$, $\mathcal{B}$, C, and $\mathcal{D}$, to represent the optimization directions. In Fig. 5, we illustrate the directions along which we vary the cavity parameters. In Table 2, we use ↑, ↓, and − to show how the output parameters change along these optimization directions. An up arrow ↑ represents an increase; a down arrow ↓ represents a decrease; a dash − represents almost no change.

The SESAM fiber laser in Fig. 1 uses a length of EDF as the gain medium. In experiments, the unsaturated gain g_0 can be increased by increasing the pump power of the EDF, the doping
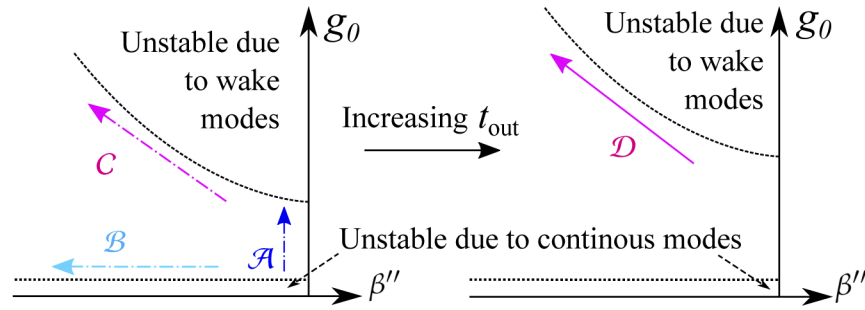
Fig. 5. To optimize the laser's output comb, we track the variation of P_{out}, τ_{out}, and I_{sb} as the parameters β'', g_0, and t_{out} vary. We show the four optimization directions $\mathcal{A}$, $\mathcal{B}$, $\mathcal{C}$, and $\mathcal{D}$. The variations of the output pulse profile are summarized in Table 2.

Table 2. The variation of the output pulse parameters along the optimization directions that we show in Fig. 5, and their comparison to the optimization goals. The up arrow ↑, the down arrow ↓, and the dash, –, indicate that the corresponding parameters increase, decrease, and remain almost unchanged, respectively.

Optimization directions	Cavity parameters			Output parameters			Do we favor this result?
	g_0	$|\beta''|$	t_{out}	P_{out}	τ_{out}	I_{sb}	
$\mathcal{A}$	↑	–	–	↑	↓	↑	No!
$\mathcal{B}$	–	↑	–	–	↑	↓	No!
$\mathcal{C}$	↑	↑	–	↑	↓	–	Yes!
$\mathcal{D}$	↑	↑	↑	↑	↓	–	**Yes!!**
Optimization goals				↑	↓	↓	

concentration, or the geometry and the length of the EDF [28]. To adjust g_0, we assume that the length of the EDF is unchanged, so that the round-trip time T_R and thus the repetition frequency $f_{FSR} = 1/T_R$ (300 MHz) are unchanged.

4.1. Directions $\mathcal{A}$ and $\mathcal{B}$ When $t_{out} = 9\%$

We first describe the change in the pulse profile and the energy fluctuation PSD, $S_w(f)$ for a fixed output coupling ratio, $t_{out} = 9\%$, corresponding to one "slice" of the parameter space that we show in Fig. 4.

In Fig. 6, we show the variation of the pulse profiles along the direction $\mathcal{A}$ in Fig. 5 for which the unsaturated gain g_0 increases while β'' remains fixed. In Fig. 6, we show results for three different values of β'', $-0.0144\,\mathrm{ps}^2$, $-0.0200\,\mathrm{ps}^2$, and $-0.0250\,\mathrm{ps}^2$. When $g_0 \geq 9.0$, the laser becomes unstable due to the wake modes when $\beta'' > -0.0144\,\mathrm{ps}^2$. When $\beta'' < -0.0144\,\mathrm{ps}^2$, the laser remains stable for some values of $g_0 > 9.0$, as we will show in Sec. 4.2. For given values of β'', we observe that P_{out} increases linearly while τ_{out} decreases as the unsaturated gain g_0 increases.

Following the direction $\mathcal{B}$ shown in Fig. 5, we decrease the anomalous group delay dispersion β'' while keeping the unsaturated gain g_0 fixed. In Fig. 6, we observe that as β'' changes from $-0.0144\,\mathrm{ps}^2$ to $-0.0250\,\mathrm{ps}^2$, P_{out} stays unchanged and τ_{out} increases by a factor of 1.6.

In Fig. 7, we show the energy fluctuation spectrum $S_w(f)$ when g_0 increases and $\beta'' = -0.0144\,\mathrm{ps}^2$. For a given energy spectrum, we define the magnitude of the sidebands I_{sb} as the difference between the peak of the wake mode sidebands and the broadband noise, as shown for the case $g_0 = 7.3$ in Fig. 7. As the unsaturated gain g_0 increases from 5.5 and approaches the stability limit $g_0 = 9.0$, we observe that the frequency offset of the sideband increases from about
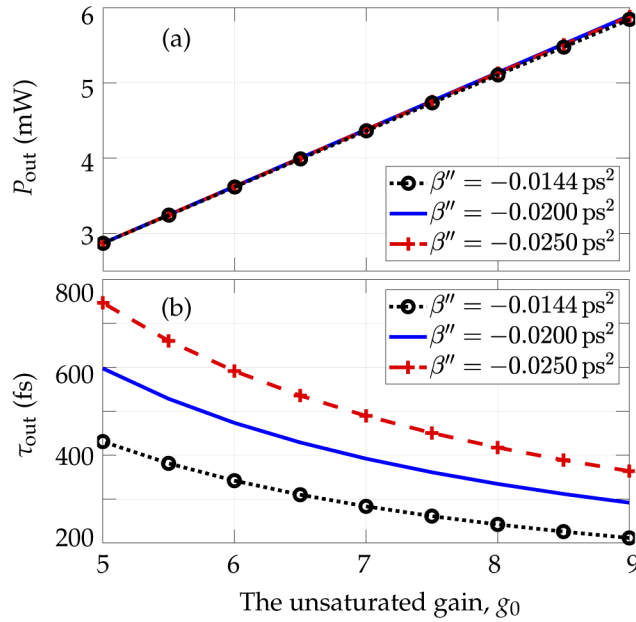
Fig. 6. (a) The average output power P_{out} and (b) the FWHM pulse duration τ_{out} as a function of the unsaturated gain g_0 for three values of the group delay dispersion β''.

7.5 MHz to above 21 MHz, and the peak magnitude of the sideband grows from nearly zero to about 10 dB/Hz above the broadband noise. The sideband profile is non-Lorentzian, which is consistent with the RF sideband spectra that we show in Fig. 3. We observe a similar decrease of the wake mode intensity following direction $\mathcal{B}$—decreasing β'' while keeping g_0 constant—as we have shown in Fig. 6.6 in [27, Chapter 6].
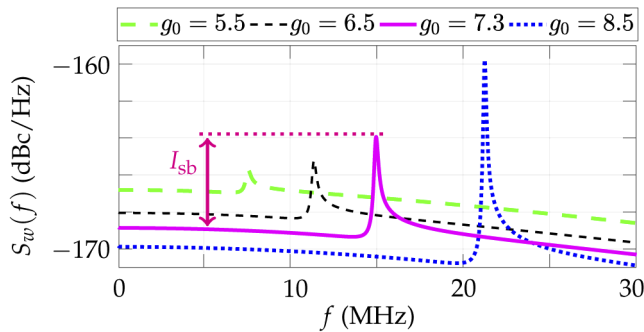

Fig. 7. The variation of the wake mode sidebands when the unsaturated gain g_0 increases for given group delay dispersion, $\beta'' = -0.0144\,\text{ps}^2$.

These observations demonstrate how the output profiles change along directions $\mathcal{A}$ and $\mathcal{B}$ in Fig. 5. We can obtain a higher-power output by increasing the pump power, but at the cost of increasing the wake mode sidebands. Alternatively, we can reduce the magnitude of the wake mode sidebands by making the group delay dispersion more negative, but at the cost of narrowing the bandwidth. Neither result satisfies our optimization goal.

4.2. Directions C and D and when t_{out} increases

The direction C in Fig. 5 follows the stability boundary of wake mode instability when the group delay dispersion β'' becomes more negative. As described in Sec. 4.1, when increasing g_0, we can obtain higher power and shorter modelocked pulses, which are desirable, but the wake mode sidebands become more pronounced, which is to be avoided. So there is a trade-off between increasing P_{out} and decreasing τ_{out} and I_{sb}. Here, we propose a level, $I_{\text{sb}} = 5\,\text{dB}$, as the acceptable magnitude for the wake mode sidebands. As an example, the case $g_0 = 7.3$ in Fig. 7 satisfies this requirement.

In Fig. 8, we show both the WMI boundary and the contour on which $I_{\text{sb}} = 5\,\text{dB}$ as β'' varies when $t_{\text{out}} = 9\%$. The case $g_0 = 7.3$ in Fig. 7 is marked as point [A] in Fig. 8.
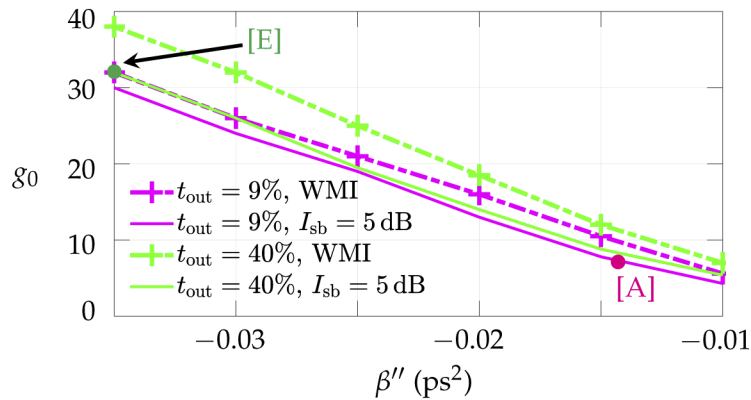

Fig. 8. The stability boundaries due to the wake mode instability (WMI) and the contours along which the magnitude of the wake mode sidebands $I_{\text{sb}} = 5\,\text{dB}$ when $t_{\text{out}} = 9\%$ and $t_{\text{out}} = 40\%$. The points [A] and [E] correspond to the cases that we show later in Fig. 10. These contour lines are located in a three-dimensional parameters space, $(g_0, \beta'', t_{\text{out}})$. Although these lines are close to each other when projected onto the (g_0, β'') plane, the difference in their corresponding output powers and pulse durations are more significant, as we show later in Figs. 9 and 10.

In practical systems, one can determine when the magnitude of wake mode sidebands is acceptable to suit the system or application requirements. When the cavity length is unchanged, one can increase the pump power to the limit at which the modelocking is destabilized by wake modes, and then decrease the pump power until the wake mode sidebands become sufficiently smaller.

In [19], we showed that we can increase P_{out} by increasing the pump power and the output coupling ratio t_{out}. Here, we adapt this technique to conduct a more comprehensive optimization. To start, in Fig. 8, we show the stability boundaries due to the WMI and the contour on which $I_{\text{sb}} = 5\,\text{dB}$ when t_{out} is set as 9% and 40%. For given values of β'', we observe that the stability limit for g_0 increases in order to compensate for the additional loss when t_{out} increases from 9% to 40%. The contours for $I_{\text{sb}} = 5\,\text{dB}$ indicate the directions C and D in Fig. 5.

In Fig. 9, we show how P_{out} and τ_{out} change along the $I_{\text{sb}} = 5\,\text{dB}$ contours for different t_{out}. We have two important observations:

1. For any given t_{out} with $I_{\text{sb}} = 5\,\text{dB}$, we observe a nearly linear increase of P_{out} while τ_{out} decreases when β'' becomes more negative. These changes are consistent with our optimization goals.

2. When t_{out} increases, we consistently obtain higher values of P_{out}. Meanwhile, the pulse duration τ_{out} slightly increases. However, the value of τ_{out} are smaller and thus improved when compared to case [A], which is obtained with the current experimental settings.
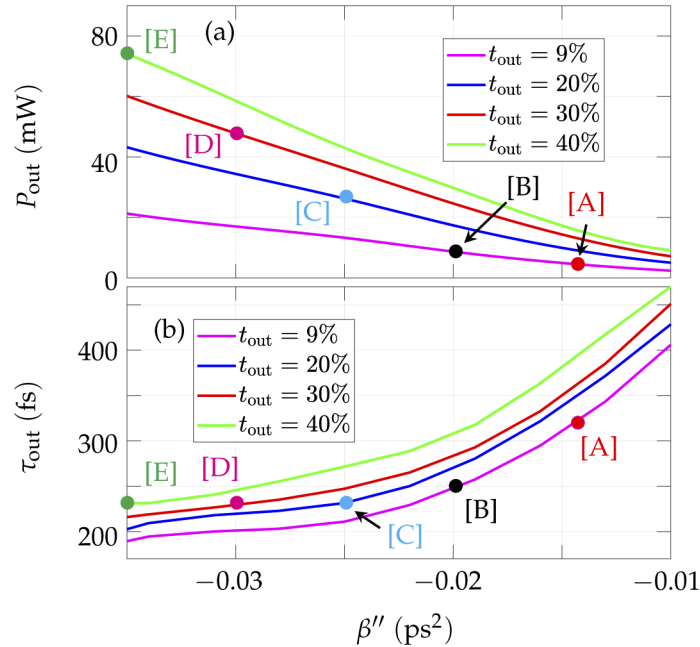

Fig. 9. When the output coupling ratio t_{out} varies, the variation of the stable pulse profile when the magnitude of the sidebands $I_{sb} = 5$ dBc. The points [A] ($g_0 = 7.3$), [B] ($g_0 = 13.0$), [C] ($g_0 = 19.0$), [D] ($g_0 = 25.3$), and [E] ($g_0 = 32.0$) correspond to the cases that we show later in Fig. 10.

The results in Fig. 9 indicate that the current experimental cavity can be modified to produce more powerful, shorter pulses with acceptable noise levels. We show a direct comparison in Fig. 10 of the output profile for cases [A], [B], [C], [D], and [E]. From case [A] to case [E], we vary the systems parameters t_{out}, β'', and g_0 following the optimization direction $\mathcal{D}$ as listed in Table 2. Figure 10(a) shows that with the $I_{sb} = 5$ dB, the average output power continues to increase from case [A] to case [E]. For case [E], the average output power is about 74 mW which is about 15 times the average power in the current experiments (about 5 mW). Meanwhile, the output pulse duration of [E] is about 180 fs, which is about 50% of the duration pulse [A].

In Fig. 10(b), we show the power spectrum of the wake mode sidebands. The 5-dB difference between the peak of the wake modes and the broadband noise is visible. In addition, from case [A] to case [E], we observe that the broadband noise relative to the signal continues to decrease. This might appear counterintuitive as higher linear loss leads to a higher absolute broadband noise level. The relative noise level that is measured in dBc/Hz decreases; the increase of the pulse energy more than compensates for the increase in the linear loss. There is a consistent improvement of the output profile as t_{out} increases despite an increase in the absolute broadband noise level.

The range of β'' that we show in Figs. 9 and 10 includes values for currently available specialty fibers with high values of anomalous dispersion [23]. In our simulations, we observe that the trend of change of the output pulse continues as $|\beta''|$ further decreases. Here, we do not study those regions with larger values of anomalous dispersion.
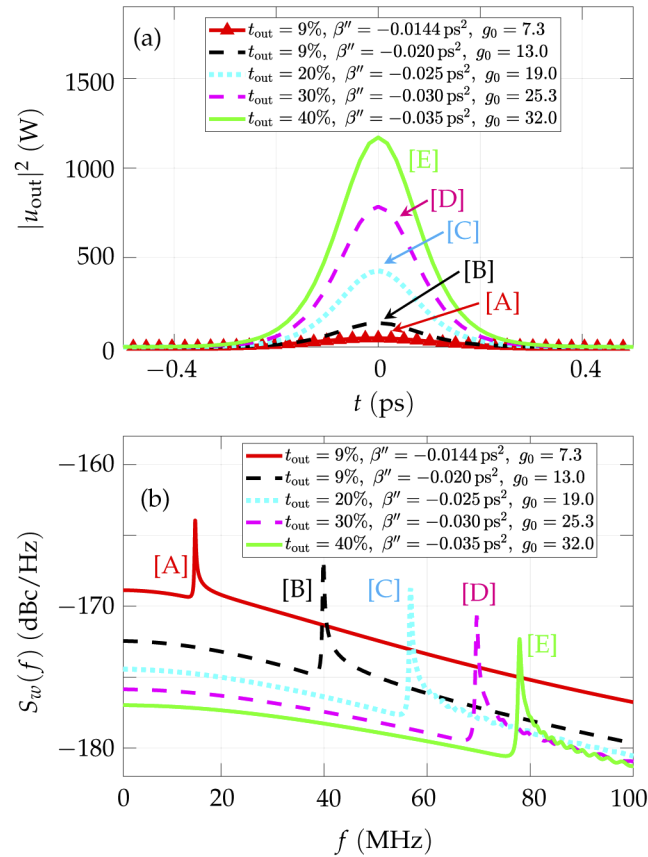
Fig. 10. The variation of (a) the stable pulse profile and the power spectrum of Δw when the power spectrum of the wake mode sidebands are less than 5 dBc above the broadband noise.

5. Verification of the optimization results

We now return to the lumped model to verify the results of the averaged model in two selected cases. The cases that we selected are for $t_{\text{out}} = 20\%$, which is approximately in the middle of the range of output couplings that we considered in our optimization. More details on the comparison of the averaged and lumped models may be found in [27].

In Sec. 4, we showed that by increasing the output coupling ratio t_{out}, we can obtain output pulses with a larger average output power and a smaller FWHM pulse duration than our reference laser, which corresponds to the current experimental system. In our optimization, we increased g_0 and β''. As we discussed in Sec. 4, we chose to vary g_0 to represent the changes in the cavity gain. In experimental systems, the cavity gain can be increased by increasing the pump power, the length of the gain fiber, or using a gain fiber that has higher doping concentration, etc, which can lead to changes in either g_0 or P_{sat}, or both. While g_0 is almost linearly proportional to P_{pump} over some range, as can be seen in Fig. 3, it is not possible to indefinitely increase g_0 by simply increasing P_{pump}. When the erbium-doped fiber is well-saturated, the unsaturated gain cannot increase indefinitely. In order to obtain a larger gain without increasing the length of the doped fiber, we increase the doping density N_e by 50% in our lumped model so that it equals 5.21×10^{25} m^{-3}. This doping density is large for an EDFA, but is within the range of EYDFAs [31]. While it is simple to make the average dispersion within a fiber laser that operates at 1550 nm more normal by using dispersion compensating fiber, the opposite is not true. However, it is

possible to make the anomalous dispersion large in magnitude by using photonic crystal fiber [23]. In our verification, we scaled the dispersion by approximately the same amount relative to the reference laser for both the averaged and lumped model.

In Table 3, we list the parameters and results of our verification study. For comparison, we also list the parameters and results for our reference laser, which we presented previously in Sec. 3. We do not list parameters that are fixed and are given in Sec. 3. As we mentioned in Sec. 3, for the case when $t_{out} = 9\%$ in Table 3, we observe that the pulse duration is smaller in the averaged model ($\tau_{out} = 254$ fs) than in the lumped model ($\tau_{out} = 311$ fs), which we also observe in the two following cases of verification.

Table 3. Input and output parameters for the reference systems [experimental (Exp.), averaged (A.), lumped (L.)] and for the two verification systems [averaged (A.), lumped (L.)].

		Reference			Verification 1		Verification 2	
		Exp.	A.	L.	A.	L.	A.	L.
Input	t_{out}	9%	9%	9%	20%	20%	20%	20%
	g_0		7.74		17.0		22.5	
	β'' (ps^2)		−0.0144		−0.025		−0.035	
	$N_e(10^{25}$ m$^{-3})$	unavailable		3.47		5.21		5.21
	β (ps^2/m)	−0.023		−0.03		−0.0534		−0.073
	P_{pump} (mW)	234		237		355		535
Output	P_{out}(mW)	4.9	4.9	4.8	23.4	18.9	31.7	28.9
	τ_{out} (fs)	300	254	311	204	321	211	286

From the comparison of the averaged and lumped models, we observe that gains in the output power predicted by the averaged model are also present in the lumped model, although they are somewhat smaller. For verification 1, the averaged model predicts an increase by a factor of 4.8, while the lumped model predicts an increase by a factor of 3.9. For verification 2, the averaged model predicts an increase by a factor of 6.5, while the lumped model predicts an increase by a factor of 6.0. In each verification, we observe that the output pulse durations predicted by the lumped model are proportionally larger than the predictions of the averaged model, which is due to the higher values of dispersion that we use in the lumped model. While the averaged model predicts a decrease of the pulse duration by about 20% for both lasers, the lumped model predicts no significant change. Both models predict that the sidebands are negligible for both lasers with a slight decrease in the optical RIN due the sufficiently high average output power of the laser.

6. Conclusion

In this paper, we have carried a computational study to optimize the cavity design of a SESAM fiber laser to increase the power output and decrease the output pulse duration without significantly increasing the sideband power or the broadband noise power relative to the output power. In prior work, we have described an approach to improve the wall plug power efficiency, which leads to a somewhat different optimization strategy [16].

We have described an optimization strategy that for the parameters that we considered yields a maximum increase in the output power of a factor of 15, while decreasing the pulse duration by a factor of two. Additionally, the sidebands in the power spectral density of the energy fluctuations remain below 5 dB, while the ratio of the signal to the broadband noise decreases. This strategy relies on simultaneously increasing the small signal gain g_0, the magnitude of the anomalous dispersion β'', and the output coupling t_{out}. Increasing $|\beta''|$ and g_0 substantially would require a significant redesign of the cavity. While it is not difficult to decrease anomalous dispersion using dispersion-compensating fiber, increasing the anomalous dispersion significantly without

changing the central wavelength requires the use of photonic crystal fiber (PCF). Polarization-maintaining and single mode photonic crystal fibers with anomalous dispersion greater than 350 ps/(nm×km) have been demonstrated [23]. However, using PCF in a laser cavity leads to additional splicing loss due to the mismatch of the mode profiles of the different fibers, which makes it more desirable to use active fibers that can provide more gain. The highest doping densities are obtained in EYDFAs. A gain of 18.5 dB (a factor of 70) over a length of 8 cm has been demonstrated [31].

Any cavity designs involve trade-offs. So, it is useful to review the design criteria that lead to a higher pulse energy and hence a higher output power without decreasing the bandwidth or increasing the intensity noise relative to the pulse. First, the pulse energy and hence the output power is largely determined by the balance between nonlinearity and dispersion. Hence, increasing the anomalous dispersion without increasing the nonlinearity makes it possible to achieve higher energy as long as there is sufficient gain in the cavity to produce the larger pulse energy. A larger dispersion also increases the range of cavity gain over which it is possible to avoid the wake mode instability while also avoiding the continuous-wave mode instability [20]. In order to avoid the continuous-wave mode instability, which can lead to chaos or multi-pulsing, the cavity loss must be greater than the gain outside the range of the few-ps gain window that is opened up by the SESAM. Increasing the gain while increasing t_{out} makes it possible to achieve high output power while at the same time ensuring that the cavity loss exceeds the gain outside the SESAM gain window. Increasing t_{out} also reduces the intracavity power that is needed to increase the output power. In our optimal designs, roughly half the increase in the output power comes from the increase in the intracavity power and roughly half comes from the increased output coupling. In this study, the modelocked laser uses a SESAM as the saturable absorber which does not help shorten the pulse duration. The output pulse duration is mainly limited by the gain filtering of the gain fiber. So, a substantial decrease in the pulse duration is difficult to achieve.

These same design criteria should apply to any modelocked fiber laser that uses a SESAM as the saturable absorber. It would be of interest in the future to apply these ideas to fiber lasers with thulium-doped fibers, which can have very high gain and operate in a spectral region in which the dispersion of standard optical fibers is twice as anomalous [32].

Our optimization used dynamical systems methods combined with an averaged model that neglected the variation of the laser parameters during one round trip in the laser and assumed that the gain spectrum is parabolic. The dynamical methods that we used made it possible to rapidly explore computationally a three-dimensional parameter space, and identify the requirements to obtain a high output power while decreasing the output pulse duration and noise. We verified the results of the optimization using a lumped model with realistic gain in two selected cases. The gains predicted by the lumped model were somewhat smaller than the gains predicted by the averaged model, but were still significant. Where the averaged model predicted a slight decrease in the pulse duration, the lumped model predicted no significant change. Both models predicted negligible sidebands and a slight decrease in the optical RIN.

In previous work, combined with the simulations that we reported in [19], we found that increasing the output coupling can increase the output power while improving the wall-plug power efficiency. In laser design, going back to the earliest lasers, it is ususally assumed that it is desirable to keep the output coupling low in order to maximize the the intra-cavity power and make good use of the gain medium. However, in a pulsed fiber laser, large intra-cavity power can lead to instabilities that are avoided by reducing the fiber length, which leads to under-utilization of the pump and poor power efficiency. From the standpoint of power efficiency, it is better to increase the gain fiber length and the output coupling. That is the case for the SESAM laser that we studied here.

Funding

Disclosures

The use of tradenames in this paper is necessary to specify experimental results and does not imply endorsement by the National Institute of Standards and Technology.

References

1. H. A. Haus, "Theory of mode locking with a fast saturable absorber," J. Appl. Phys. **46**(7), 3049–3058 (1975).
2. H. Haus and M. Islam, "Theory of the soliton laser," IEEE J. Quantum Electron. **21**(8), 1172–1188 (1985).
3. S. A. Diddams, "The evolving optical frequency comb [invited]," J. Opt. Soc. Am. B **27**(11), B51–B62 (2010).
4. N. R. Newbury, "Searching for applications with a fine-tooth comb," Nat. Photonics **5**(4), 186–188 (2011).
5. I. Hartl, G. Imeshev, G. Cho, M. Fermann, T. Schibli, K. Minoshima, A. Onae, F.-L. Hong, H. Matsumoto, J. Nicholson, and M. Yan, "Carrier envelope phase locking of an in-line, low-noise Er fiber system," in *Advanced Solid-State Photonics*, (Optical Society of America, 2004), p. PDP10.
6. T. R. Schibli, K. Minoshima, F.-L. Hong, H. Inaba, A. Onae, H. Matsumoto, I. Hartl, and M. E. Fermann, "Frequency metrology with a turnkey all-fiber system," Opt. Lett. **29**(21), 2467–2469 (2004).
7. S. Droste, G. Ycas, B. R. Washburn, I. Coddington, and N. R. Newbury, "Optical frequency comb generation based on erbium fiber lasers," Nanophotonics **5**(2), 196–213 (2016).
8. B. R. Washburn, S. A. Diddams, N. R. Newbury, J. W. Nicholson, M. F. Yan, and C. G. Jørgensen, "Phase-locked, erbium-fiber-laser-based frequency comb in the near infrared," Opt. Lett. **29**(3), 250–252 (2004).
9. E. A. Avrutin, J. H. Marsh, and E. L. Portnoi, "Monolithic and multi-gigahertz mode-locked semiconductor lasers: constructions, experiments, models and applications," IEE Proc.: Optoelectron. **147**(4), 251–278 (2000).
10. W. S. E. U. Rafailov and M. A. Cataluna, "Mode-locked quantum-dot lasers," Nat. Photonics **1**(7), 395–401 (2007).
11. L. C. Sinclair, I. Coddington, W. C. Swann, G. B. Rieker, A. Hati, K. Iwakuni, and N. R. Newbury, "Operation of an optically coherent frequency comb outside the metrology lab," Opt. Express **22**(6), 6996–7006 (2014).
12. S. M. Schweyer, B. Eder, P. Putzer, M. Mayerbacher, N. Lemke, K. U. Schreiber, U. Hugentobler, and R. Kienberger, "All-in-fiber SESAM based comb oscillator with an intra-cavity electro-optic modulator for coherent high bandwidth stabilization," Opt. Express **26**(18), 23798–23807 (2018).
13. D. Waldburger, S. M. Link, M. Mangold, C. G. E. Alfieri, E. Gini, M. Golling, B. W. Tilma, and U. Keller, "High-power 100 fs semiconductor disk lasers," Optica **3**(8), 844–852 (2016).
14. H. Byun, M. Y. Sander, A. Motamedi, H. Shen, G. S. Petrich, L. A. Kolodziejski, Erich P. Ippen, and F. X. Kärtner, "Compact, stable 1 GHz femtosecond Er-doped fiber lasers," Appl. Opt. **49**(29), 5577–5582 (2010).
15. S. Wang, C. R. Menyuk, L. Sinclair, I. Coddington, and N. R. Newbury, "Soliton wake instability in a SESAM modelocked fiber laser," in *CLEO: 2014*, (Optical Society of America, 2014), p. SW3E.4.
16. S. Wang, S. Droste, L. C. Sinclair, I. Coddington, N. R. Newbury, T. F. Carruthers, and C. R. Menyuk, "Wake mode sidebands and instability in mode-locked lasers with slow saturable absorbers," Opt. Lett. **42**(12), 2362–2365 (2017).
17. F. Kärtner, I. Jung, and U. Keller, "Soliton mode-locking with saturable absorbers," IEEE J. Sel. Top. Quantum Electron. **2**(3), 540–556 (1996).
18. S. Wang, C. R. Menyuk, S. Droste, L. Sinclair, I. Coddington, and N. R. Newbury, "Wake mode sidebands and instability in comb lasers with slow saturable absorbers," in *Conference on Lasers and Electro-Optics*, (Optical Society of America, 2016), p. SM3H.5.
19. S. Wang, C. R. Menyuk, S. Droste, L. Sinclair, I. R. Coddington, and N. Newbury, "Optimizing the power efficiency of a SESAM fiber comb laser," in *Conference on Lasers and Electro-Optics*, (Optical Society of America, 2017), p. SF1C.2.
20. S. Wang, A. Docherty, B. S. Marks, and C. R. Menyuk, "Boundary tracking algorithms for determining the stability of mode-locked pulses," J. Opt. Soc. Am. B **31**(11), 2914–2930 (2014).
21. C. R. Menyuk and S. Wang, "Spectral methods for determining the stability and noise performance of passively modelocked lasers," Nanophotonics **5**(2), 332–350 (2016).
22. S. Wang, T. F. Carruthers, and C. R. Menyuk, "Efficiently modeling the noise performance of short-pulse lasers with a computational implementation of dynamical methods," J. Opt. Soc. Am. B **35**(10), 2521–2531 (2018).
23. M. Y. Chen, H. Subbaraman, and R. T. Chen, "One stage pulse compression at 1554nm through highly anomalous dispersive photonic crystal fiber," Opt. Express **19**(22), 21809–21817 (2011).
24. H. Haus and A. Mecozzi, "Noise of mode-locked lasers," IEEE J. Quantum Electron. **29**(3), 983–996 (1993).
25. S. Wang, A. Docherty, B. S. Marks, and C. R. Menyuk, "Comparison of numerical methods for modeling laser mode locking with saturable gain," J. Opt. Soc. Am. B **30**(11), 3064–3074 (2013).
26. S. K. Turitsyn, B. G. Bale, and M. P. Fedoruk, "Dispersion-managed solitons in fibre systems and lasers," Phys. Rep. **521**(4), 135–203 (2012). Dispersion-Managed Solitons in Fibre Systems and Lasers.

27. S. Wang, "Analysis of Stability and Noise in Passively Modelocked Comb Lasers," Ph.D. dissertation, (University of Maryland, Baltimore County 2018).

28. C. R. Giles and E. Desurvire, "Modeling erbium-doped fiber amplifiers," J. Lightwave Technol. **9**(2), 271–283 (1991).

29. V. S. Grigoryan and C. R. Menyuk, "Dispersion-managed solitons at normal average dispersion," Opt. Lett. **23**(8), 609–611 (1998).

30. M. F. Limonov, M. V. Rybin, A. N. Poddubny, and Y. S. Kivshar, "Fano resonances in photonics," Nat. Photonics **11**(9), 543–554 (2017).

31. N. G. Boetti, G. C. Scarpignato, J. Lousteau, D. Pugliese, L. Bastard, J.-E. Broquin, and D. Milanese, "High concentration Yb-Er co-doped phosphate glass for optical fiber amplification," J. Opt. **17**(6), 065705 (2015).

32. Z. Li, A. M. Heidt, J. M. O. Daniel, Y. Jung, S. U. Alam, and D. J. Richardson, "Thulium-doped fiber amplifier for optical communications at 2μm," in *2013 Optical Fiber Communication Conference and Exposition and the National Fiber Optic Engineers Conference (OFC/NFOEC)*, (2013), pp. 1–3.